Journal of Cranio-Maxillo-Facial Surgery xxx (xxxx) xxx

Contents lists available at ScienceDirect

Journal of Cranio-Maxillo-Facial Surgery

journal homepage: www.jcmfs.com

Preoperative imaging in third molar surgery — A prospective comparison of X-ray-based and radiation-free magnetic resonance orthopantomography

Adib Al-Haj Husain [a,b,1], Dominik A. Oechslin [a,1], Bernd Stadlinger [a], Sebastian Winklhofer [b], Mutlu Özcan [c,d], Daphne Schönegg [e], Nadin Al-Haj Husain [c,d,f], Stefan Sommer [g,h,i], Marco Piccirelli [b,1], Silvio Valdec [a,*,1]

[a] Clinic of Cranio-Maxillofacial and Oral Surgery, Center of Dental Medicine, University of Zurich, Zurich, Switzerland
[b] Department of Neuroradiology, Clinical Neuroscience Center, University Hospital Zurich, University of Zurich, Zurich, Switzerland
[c] Division of Dental Biomaterials, Clinic of Reconstructive Dentistry, Center of Dental Medicine, University of Zurich, Zurich, Switzerland
[d] Clinic of Masticatory Disorders, Orofacial Pain Unit, Center of Dental Medicine, University of Zurich, Zurich, Switzerland
[e] Department of Oral and Cranio-Maxillofacial Surgery, University Hospital Basel, University of Basel, Basel, Switzerland
[f] Department of Reconstructive Dentistry and Gerodontology, School of Dental Medicine, University of Bern, Bern, Switzerland
[g] Siemens Healthineers International AG, Zurich, Switzerland
[h] Swiss Center for Musculoskeletal Imaging (SCMI), Balgrist Campus, Zurich, Switzerland
[i] Advanced Clinical Imaging Technology (ACIT), Siemens Healthcare AG, Lausanne, Switzerland

ARTICLE INFO

Handling Editor: Prof. Emeka Nkenke

Keywords:
MeSH): diagnostics
Magnetic resonance imaging
Orthopantomography
Panoramic radiography
Third molar surgery
Third molar
Wisdom teeth
Dental MRI

ABSTRACT

This study aimed to compare preoperative data relevant to third molar surgery based on radiographic orthopantomography (OPG) and orthopantomogram-like MR images (MR-OPG), using five different MR protocols.

X-ray-based OPG and OPG-like MRI reconstructions from DESS, SPACE-STIR, SPACE-SPAIR, T1-VIBE-Dixon, and UTE sequences were acquired in 11 patients undergoing third molar surgery, using a 15-channel mandibular coil. Qualitative (image quality, susceptibility to artifacts, positional relationship, contact/non-contact of the inferior alveolar nerve (IAN), relationship to maxillary sinus, IAN continuity, root morphology) and quantitative (tooth length, retromolar distance, distance to the IAN, and distance to the mandible margin) parameters of the maxillary and mandibular third molars were assessed regarding inter-reader agreement and quantitative discrepancies by three calibrated readers.

Radiation-free MR-OPGs generated within clinically tolerable acquisition times, which exhibited high image quality and low susceptibility to artifacts, showed no significant differences compared with X-ray-based OPGs regarding the assessment of quantitative parameters. UTE MR-OPGs provided radiographic-like images and were best suited for assessing qualitative preoperative data (positional relationship, nerve contact/non-contact, and dental root morphology) relevant to third molar surgery. For continuous and focal nerve imaging, DESS MR-OPG was superior.

MR-OPGs could represent a shift towards indication-specific and modality-oriented perioperative imaging in high-risk oral and maxillofacial surgery.

1. Introduction

Accurate identification of the positional relationship between the inferior alveolar nerve and the roots of the mandibular third molars by means of diagnostic imaging prior to third molar surgery is crucial for the success of the procedure, especially for avoidance of iatrogenic nerve injuries (Jerjes et al., 2006; Qi et al., 2019). With its short radiation exposure time and dose (4–30§µSv) it is suitable for routine evaluation of tooth angulation, number and shape of the roots, and proximity of the root apices to the osseous boundaries of the mandibular canal. Given the fact that orthopantomography (OPG) offers a two-dimensional overview only, its limitations are obvious. Therefore, in complex cases where OPG

* Corresponding author. Clinic of Cranio-Maxillofacial and Oral Surgery, Center of Dental Medicine, University of Zurich, Plattenstrasse 11, 8032, Zurich, Switzerland.
E-mail address: silvio.valdec@zzm.uzh.ch (S. Valdec).
[1] These authors contributed equally to this work.

https://doi.org/10.1016/j.jcms.2023.10.005
Received 4 April 2023; Received in revised form 31 July 2023; Accepted 15 October 2023
Available online 20 October 2023

shows radiographic risk signs, such as superimposition, darkening of the roots, and noncontinuous cortical integrity or diversion of the mandibular canal, three-dimensional imaging by cone-beam computed tomography (CBCT) is justified, albeit with a higher radiation exposure of 18–200 μSv (Dula et al., 2014).

In addition to the fact that soft tissues cannot be directly visualized with conventional X-ray imaging techniques, increased exposure to diagnostic X-rays in dentistry results in an increased risk of radiation-induced cancers of the head and neck region, with the thyroid and salivary glands being most affected by the development of neoplasms (Hwang et al., 2018). Given the lifetime exposure to X-rays from biomedical imaging, this poses a particular risk to highly radiosensitive, genetically susceptible young adults (Tsapaki, 2017; Hwang et al., 2018).

Thanks to recently introduced technical innovations and advanced imaging protocols, radiation-free magnetic resonance imaging (MRI), with its superior soft-tissue contrast resolution, has opened up a wide range of new diagnostic possibilities in the dental field. In dental MRI of the oral cavity, simultaneous visualization of cortical bone, dental tissue, and the inferior alveolar neurovascular bundle is challenging because of the complex anatomy of the mandibular third molar region (Al-Haj Husain et al., 2022b). Due to the limited molecular motion of the hydrogen nuclei of dental and cortical bone tissue, and the fast signal decay after radiofrequency excitation, conventional MRI protocols, such as gradient return echo (GRE) or fast spin echo (FSE), do not provide adequate visualization (Idiyatullin et al., 2011; Chang et al., 2015).

Black bone MRI sequences, such as 3D double-echo steady-state (DESS) and 3D short tau inversion recovery (STIR), have provided highly confidential quantitative and qualitative preoperative assessment of the mandibular third molar region. Compared with conventional radiographic 3D imaging (e.g. CBCT), they have even offered advantages in the early detection of inflammatory processes and continuous visualization of the inferior alveolar nerve and lingual nerve (Burian et al., 2019; Valdec et al., 2021; Al-Haj Husain et al., 2022c). However, motion artifacts and artifacts due to dental restorations may compromise image quality, which could be further minimized by the use of dedicated technical tools for image acquisition, such as intraoral coils (Ludwig et al., 2016), radiofrequency coils (Prager et al., 2015), or mandibular coils (Al-Haj Husain et al., 2022a), with the latter allowing faster imaging by parallel imaging and consecutive k-space undersampling. By using multiplanar reconstruction, orthopantomogram-like MR images (MR-OPG) can be generated from imaging datasets.

Since OPG assessment is an integral part of dental education and the most familiar imaging modality in routine dental practice, we wanted to combine this experience in OPG interpretation with the advantages of a neuroradiological evaluation of head and neck MRI. Therefore, our radiological pilot study aimed to compare qualitative parameters (technical image quality, susceptibility to artifacts, and reliability of the positional relationship between the inferior alveolar nerve or the bony boundaries of the maxillary sinus and the roots of the third molars) and quantitative parameters (evaluation of distances, such as tooth lengths, retromolar distance, distance to the inferior alveolar nerve, and distance to the margin of the mandible) in patients undergoing third molar surgery, based on radiographic OPG and MR-OPG, using black bone MRI sequences (DESS, SPACE STIR and spectral attenuated inversion recovery (SPACE SPAIR), volumetric interpolated breath-hold examination (T1-VIBE-Dixon) and ultrashort echo time (UTE) prototype sequences, and a 15-channel mandibular coil to provide potential evidence for implementation in perioperative imaging sequences in oral and maxillofacial surgery.

2. Materials and methods

2.1. Study design and setup

To investigate the feasibility of MR-OPGs in third molar surgery, this prospective clinical feasibility study recruited patients with an indication for third molar removal, who were admitted to the Clinic of Cranio-Maxillofacial and Oral Surgery in the Center of Dental Medicine, University of Zurich, Switzerland. From June 2022 to October 2022, consecutive patients were recruited from routine daily clinical practice. Male or female patients between the ages of 18 and 70 years, who had a clinical or radiological indication for third molar surgery, were enrolled in the study. Patients with local acute infection, mandibular nerve damage, pregnancy, or a general contraindication for MR imaging were excluded. After the initial clinical examination, all study participants underwent an X-ray-based OPG, acquired preoperatively by trained research personnel of the Clinic of Cranio-Maxillofacial and Oral Surgery. Afterwards, MRI data acquisition was performed by trained neuroradiologists and research staff in the Department of Neuroradiology of the University Hospital Zurich, University of Zurich, Switzerland. Oral surgeons performed the consecutive surgical interventions on the third molars, under local anesthesia.

The study (2022-D0090) was approved by the Cantonal Ethics Commission of Zurich (Switzerland). All participants gave their written informed consent to participate in the study, in line with the Declaration of Helsinki and its later revised ethical standards.

2.2. Image acquisition

OPGs were obtained in the standing position, with the head oriented to the Frankfurt horizontal occlusal plane, using a Cranex 3D (Soredex, KaVo, Biberach, Germany). Dental MRI protocols were acquired with a 3-T scanner (MAGNETOM Skyra, release VE11E; Siemens Healthineers, Erlangen, Germany) and a 15-channel mandibular coil (NORAS MRI products, Hoechberg, Germany). The acquired protocols included 3D-

Table 1
MRI sequence parameters. Orthopantomogram-like MR images (MR-OPG) were obtained using 3D double-echo steady-state (DESS), 3D turbo spin echo short-tau inversion recovery (T2 SPACE STIR), 3D turbo spin echo spectrally attenuated inversion recovery (T2 SPACE SPAIR), volumetric interpolated breath-hold examination (T1 VIBE-Dixon), and ultrashort echo time (UTE).

Pulse sequence	DESS	T2 SPACE STIR	T2 SPACE SPAIR	T1 Vibe Dixon	UTE
Dimension of acquisition	3D	3D	3D	3D	3D radial
Slabs/slices	1/104	1/120	1/120	1/96	1/384
TR [ms]	11.16	3300	3300	5.81	4.62
TE [ms]	4.21	113	115	2.46/3.69	0.04
Flip angle [degrees]	30	T2 var	T2 var	11	5
Bandwidth [Hz/Px]	355	425	425	660/700	1184
Fat suppression	Water excit. Normal	None	SPAIR, strong	Dixon, optim inphase	None
FoV read and phase [mm]	242 × 242	190 × 190	190 × 190	380 × 212	230 × 230
Phase encoding direction	R » L	A » P	A » P	F » H	A » P
Matrix read/phase	320 × 320	256 × 256	256 × 256	380 × 380	384 × 384
Slice thickness [mm]	0.75	0.75	0.75	1.00	0.6
Average	1	1.4	1.4	1	1
Time of acquisition [min:s]	12:24	12:36	12:36	05:28	03:07

DESS, 3D-SPACE STIR, 3D-SPACE SPAIR, T1-VIBE-Dixon, and prototype UTE sequence. All sequences were acquired with sub-millimeter isotropic resolution and after a quality-optimizing pilot. More detailed technical scan parameters are shown in Table 1.

2.3. Image analysis

MRI data were stored, processed, and analyzed in syngo. via (release VB60A; Siemens Healthineers, Erlangen, Germany). Prior to evaluation, image post-processing included curved multiplanar reconstruction (MPR) of the acquired datasets for each MRI protocol to generate MR-OPGs with a slice thickness of 0.5 mm. MR-OPG reconstructions were created manually, by a single calibrated examiner (AAH), performing the reconstruction planning through the occlusal plane. The evaluation was performed on a 2-megapixel high-resolution liquid-crystal display.

MR-OPGs reconstructed from the 3D-DESS, 3D-STIR, 3D-SPAIR, T1-VIBE-Dixon, and UTE datasets were evaluated in random order by three readers with different levels of experience (reader A, resident oral surgeon with 5 years' experience, reader B, resident oral surgeon with 2 years' experience who did not meet MR-OPGs during everyday work, reader C, attending board-certified radiologist and neuroradiologist, with 6 years' experience in general radiology and 30 years' experience in neuroradiology). All readers conducted a calibration session prior to their evaluation, in which two random cases were evaluated together to eliminate any uncertainties. This was followed by an evaluation of inter-reader agreement, with readers not knowing each other's readouts. Qualitative analysis was conducted using a Likert rating scale to assess the general technical image quality and the occurrence of artifacts. In addition, the continuous visibility of the inferior alveolar nerve in the surgical site, the classification of the positional relationship between the third molar and adjacent anatomical structures, and the root morphology were evaluated. Quantitative analysis included evaluation of the distances between the most superior aspect of the occlusal surface of the dental crown of the third molars and the most apical point of the root, measurement of the retromolar space, and the distance from the most superior aspect of the occlusal surface of the dental crown to the inferior alveolar nerve or the cortical boundaries of the inferior alveolar canal, and the distance to the edge of the mandible.

2.4. Qualitative readout

Overall technical image quality was graded using a modified 5-point Likert scale (Guggenberger et al., 2012): 4, excellent image quality with full diagnostic interpretability; 3, good image quality with full diagnostic interpretability; 2, satisfactory image quality and diagnostic interpretability; 1, markedly reduced image quality and impaired diagnostic interpretability; 0, severely reduced image quality, allowing no diagnostic interpretability.

Based on the significance of the artifacts in the third molar region, the following modified 5-point Likert scale (Guggenberger et al., 2012) was used to evaluate the occurrence of motion artifacts, pulsation, and ghosting: 4, no artifacts; 3, mild artifacts; 2, moderate artifacts; 1, severe artifacts; 0, non-diagnostic.

To analyze nerve continuity, the inferior alveolar nerve was divided into proximal (from the mandibular foramen to the third molar) and distal (from the third molar to the first molar) portions and assessed for continuous visibility using a modified 5-point Likert scale according to Al-Haj Husain et al. (Al-Haj Husain et al., 2022c): 4, excellent = both the proximal and distal portions of the nerve identified continuously; 3, good = both the proximal and distal portions of the nerve identified but not continuously; 2, medium = only the proximal portion of the nerve continuously identified; 1, poor = only the proximal portion of the nerve identified but not continuously; 0, none = nerve not identified.

In conventional OPG and MR-OPG, the positional relationship of the maxillary third molars was evaluated according to the classification of Jung et al. (Jung and Cho, 2015): 1, sinus floor above the roots; 2, sinus floor touching the root tips; 3, sinus floor superimposed on up to one third of the root; 4, sinus floor superimposed on up to two thirds of the root; 5, sinus floor extending up to the cervical margin of the tooth.

The position of the mandibular molars was classified in terms of: (i) the depth of impaction (Pell and Gregory classification (Pell and Gregory, 1933)): A, occlusal plane of the impacted third molar at the same level as the occlusal plane of the second molar; B, highest part of the occlusal plane of the impacted third molar located between the occlusal plane and the cementoenamel junction of the second molar; C, highest part of the occlusal plane of the impacted third molar located below the cervical line of the second molar); (ii) the ramus relationship (Pell and Gregory classification (Pell and Gregory, 1933)): I, sufficient space between the ascending ramus and distal side of the second molar for third molar eruption; II, space available, but ascending ramus covering the distal portion of the third molar; III, lack of space, the third molar completely embedded in the ascending ramus bone), and (iii) the angulation of the third molar to the long axis of the second molar (Winter Classification (Winter, 1926)): 1, vertical angulation; 2, horizontal angulation; 3, distoangular angulation; 4, mesioangular angulation; 5, transversal angulation; 6, others). In addition, position was also assessed according to whether there was a contact or non-contact situation between the inferior alveolar nerve and the mandibular third molar. Root morphology was also assessed by evaluating the curvature of the roots according to the following classification: 1, straight roots; 2, both distally curved; 3, distal root distally curved; 4, both roots curved towards each other; 5, mesial roots distally curved; 6, distal root mesially curved.

2.5. Quantitative readout

Quantitative parameters relevant to the surgical assessment of the preoperative situation and the imaging accuracy of MR-OPGs were evaluated where the tooth length from the highest point of the occlusal plane to the most apical point of the third molar was assessed. In addition, the distance from the third molar to the mandibular body margin, and the retromolar space, defined as the line from the anterior margin of the mandibular ramus to the mandibular or maxillary second molar, were measured (Yilmaz et al., 2016). In order to assess the reliability of the measurements, a single calibrated examiner (AAH) repeated the morphometric measurements after 2 weeks to avoid recall bias. If the second measurement differed from the first, an average of both measurements was calculated. In unclear cases, these were clarified by a discussion between all three readers.

2.6. Statistical analysis

Statistical analyses were conducted using IBM SPSS Statistics software (version 26.0; IBM Corp., Armonk, NY, USA). Descriptive statistics were used to calculate scores for image quality, artifacts, and inferior alveolar nerve continuity to obtain metric variables with means, standard deviations, and medians for each reader and MR protocol. In addition, the average of all values was calculated. Inter-reader agreement was determined for the following variables: image quality, artifacts, inferior alveolar nerve continuity score, root morphology, nerve contact/non-contact determination, impaction depth, ramus relationship, angulation of the third molar to the second molar, and positional relationship. Inter-reader agreement was evaluated by analyzing the intraclass correlation coefficient (ICC) type 2:1 and the 95% confidence interval (CI) based on absolute agreement according to the 2-way random model. On the basis of the selected 95% CI, the ICC values and, consequently, the agreement beyond chance could be interpreted as follows: poor, <0.5; moderate, 0.5–0.75; good, 0.75–0.9; and excellent, >0.9 (Koo and Li, 2016). For quantitative parameters, test of homogeneity, two-way ANOVA, and Tukey's Post-hoc tests were performed to assess statistically significant differences between conventional OPGs and MR-OPGs regarding the tested variables. All statistical analyses were conducted on a significance level of $\alpha = 0.05$.

3. Results

In total, 11 patients were included in this study, with a total of 31 third molars analyzed. The cohort group included eight males (73%) and three females (27%), with a mean age of 36.27 ± 15 years (median age, 36 years; age range, 22–67 years).

3.1. Qualitative results

The mean score of all readers for image quality was excellent, with full diagnostic interpretability, for UTE (3.64 ± 0.498) and good for VIBE (3.09 ± 1.036), while it was lowest for SPACE STIR (2.837 ± 1.049). Artifacts due to motion, pulsation, and ghosting were most prevalent in SPACE STIR (2.76 ± 1.028) and SPACE SPAIR (2.76 ± 1.154), whereas the UTE sequence (3.15 ± 0.815) was generally devoid of artifacts.

Nerve continuity analysis yielded excellent results, with the entire course of the inferior alveolar nerve consistently visible in all cases for DESS and SPACE STIR (both 4 ± 0). In contrast, the VIBE and UTE protocols yielded the lowest visibility, with mean scores of 3.56 ± 0.717 and 3.64 ± 0.79, respectively (Table 2).

3.2. Quantitative results

The homogeneity test based on the Kolmogorov-Smirnov statistic revealed a homogeneous distribution ($p = 0.092$). No significant differences were registered between X-ray based and MR-OPG (DESS, SPACE STIR, SPACE SPAIR, UTE all $p = 1$, VIBE-Dixon $p = 0.99$) regarding all parameters – tooth length of the third molar, retromolar space (maxilla), retromolar space (mandible), distance from the third molar to the inferior alveolar nerve canal, and distance from the third molar to the mandibular body margin. The discrepancy between both imaging modalities was estimated to be correspondingly small (≤0.25 mm) and showed no statistical significance ($p = 0.68$).

3.3. Inter-reader agreement

The inter-reader agreement between readers A, B, and C in terms of image quality was excellent in DESS MR-OPG (ICC = 1; $\boldsymbol{p} < 0.001$), VIBE (ICC = 0.945; $\boldsymbol{p} < 0.001$), and SPACE SPAIR (ICC = 0.93; $\boldsymbol{p} < 0.001$), while UTE (ICC = 0.959; $\boldsymbol{p} < 0.001$), SPACE SPAIR (ICC = 0.952; $\boldsymbol{p} < 0.001$), and VIBE (ICC = 0.939; $\boldsymbol{p} < 0.001$) showed the best inter-reader agreement in the assessment of artifacts. In the evaluation of root morphology, perfect agreement was obtained between the readers in UTE (ICC = 1) and VIBE (ICC = 1) MR sequences, while SPACE SPAIR (ICC = 0.647; $\boldsymbol{p} < 0.001$) showed the lowest agreement.

Of the parameters relevant in the preoperative diagnosis of mandibular third molars, inferior alveolar nerve continuity agreement was the best in DESS, SPACE STIR, SPACE SPAIR, and UTE (all ICC = 1), while the inter-reader agreement in VIBE MR-OPG could still be considered excellent (ICC = 0.983; $\boldsymbol{p} < 0.001$). Inter-reader agreement for contact and noncontact analysis of the inferior alveolar nerve was perfect for all MR sequences (all ICC = 1), while impaction depth was perfect for UTE (ICC = 1), and the assessment of the ramus relationship was excellent for SPACE STIR, SPACE SPAIR, and VIBE (all ICC = 1) and excellent for UTE (ICC = 0.982; $\boldsymbol{p} < 0.001$) and DESS (ICC = 0.972; $\boldsymbol{p} < 0.001$). In the preoperative radiological assessment of the positional relationship of maxillary third molars, UTE, VIBE, and SPACE SPAIR achieved perfect inter-reader agreement (ICC = 1) and excellent agreement for DESS (ICC = 0.955; $\boldsymbol{p} < 0.001$) and SPACE STIR (0.965; $\boldsymbol{p} < 0.001$). More detailed information can be found in Table 3.

4. Discussion

The outcomes of our study demonstrate that the latest advances in MRI technology with high-field MR scanners, dedicated MR sequences, and newly developed hardware, such as the 15-channel mandibular coil, allow the acquisition of MR-OPGs for preoperative diagnosis in third molar surgery within clinically tolerable acquisition times (from 3 to 12 min). The acquired MR-OPGs offered no significant disadvantages in terms of quantitative and qualitative parameters compared with conventional OPGs, and even provided beneficial information, enabling simultaneous visualization of mineralized biological hard and soft tissue, with high resolution and contrast. The results obtained in this study were very robust and highly reproducible, independent of the observers' experience. The inter-reader agreement for reader B was selected to determine the expected lower limit for non-experts in MRI reading, who do not have much experience with MRI reading in everyday clinical practice, to evaluate the applicability of MR-OPGs in routine dental practice.

The applied T2-weighted black bone MRI sequences (DESS, SPACE STIR, and SPACE SPAIR) provided robust images, with good-to-excellent signal-to-noise ratio (SNR) of the inferior alveolar nerve in the region of interest, confirming the results from the literature (Al-Haj Husain et al., 2021b) that support their use for visualization of normal nerve anatomy as well as pathological changes of its branches and fascicular bundles (Andreisek and Chhabra, 2015). The best delineation of the inferior alveolar nerve with high diagnostic confidence and good inter-reader reliability was found with the DESS and SPACE-STIR protocols, confirming previously published data (Fujii et al., 2015; Burian et al., 2020a; Al-Haj Husain et al., 2021b).

DESS MR-OPG could be considered the most appropriate protocol for

Table 2
Average scores for the three readers (A: experienced chief resident oral surgeon; B: resident oral surgeon; C: experienced board-certified neuroradiologist) in evaluating overall image quality (4 = excellent, 0 = severely reduced image quality), susceptibility to artifacts (4 = no artifacts, 0 = non-diagnostic), and continuity of the inferior alveolar nerve (4 = excellent, 0 = none), using 5-point Likert scales.

	MRI sequence	Reader A	Reader B	Reader C	Average
Image quality (mean ± SD (median))	DESS	3 ± 1.265 (3)	3 ± 1.265 (3)	3 ± 1.265 (3)	3 ± 1.265
	SPACE STIR	2.82 ± 0.874 (3)	2.96 ± 1.168 (3)	2.73 ± 1.104 (3)	2.837 ± 1.049
	SPACE SPAIR	2.91 ± 1.136 (3)	3.09 ± 1.221 (3)	2.91 ± 1.136 (3)	2.97 ± 1.164
	VIBE	3.09 ± 0.944 (3)	3.18 ± 0.982 (3)	3 ± 1.183 (3)	3.09 ± 1.036
	UTE	3.64 ± 0.505 (4)	3.73 ± 0.467 (4)	3.55 ± 0.522 (4)	3.64 ± 0.498
Artifacts (mean ± SD (median))	DESS	3 ± 1.183 (3)	2.91 ± 1.3 (3)	3 ± 1.183 (3)	3 ± 1.222
	SPACE STIR	2.82 ± 0.982 (3)	2.82 ± 0.982 (3)	2.64 ± 1.12 (3)	2.76 ± 1.028
	SPACE SPAIR	2.82 ± 1.168 (3)	2.73 ± 1.191 (3)	2.73 ± 1.104 (3)	2.76 ± 1.154
	VIBE	2.91 ± 0.831 (3)	3 ± 0.894 (3)	2.91 ± 0.831 (3)	2.94 ± 0.842
	UTE	3.18 ± 0.751 (3)	3.09 ± 0.944 (3)	3.18 ± 0.751 (3)	3.15 ± 0.815
Inferior alveolar nerve continuity score (mean ± SD (median))	DESS	4 ± 0 (4)	4 ± 0 (4)	4 ± 0 (4)	4 ± 0
	SPACE STIR	4 ± 0 (4)	4 ± 0 (4)	4 ± 0 (4)	4 ± 0
	SPACE SPAIR	3.81 ± 0.512 (4)	3.73 ± 0.647 (4)	3.73 ± 0.647 (4)	3.757 ± 0.602
	VIBE	3.64 ± 0.658 (4)	3.59 ± 0.666 (4)	3.45 ± 0.82 (4)	3.56 ± 0.717
	UTE	3.64 ± 0.79 (4)	3.64 ± 0.79 (4)	3.64 ± 0.79 (4)	3.64 ± 0.79

Table 3
Inter-reader agreement for the three readers (A: experienced chief resident oral surgeon; B: resident oral surgeon; C: experienced board-certified neuroradiologist) regarding qualitative parameters relevant for third molar surgery, assessed using intraclass correlation coefficient (ICC) type 2:1 and a 95% confidence interval (CI), based on absolute agreement according to a two-way random model.

Agreement	MRI Sequence	Reader A and B	Reader B and C	Reader C and A	Average
Image quality (ICC (95% CI); *p*–value)	DESS	1	1	1	1
	SPACE STIR	0.826 (0.467–0.95); $p < 0.001$	0.965 (0.881–0.99); $p < 0.001$	0.861 (0.727–0.980); $p < 0.001$	0.884 (0.692–0.973)
	SPACE SPAIR	0.935 (0.781–0.982); $p < 0.001$	0.927 (0.72–0.967); $p < 0.001$	0.929 (0.757–0.980); $p < 0.001$	0.93 (0.753–0.976)
	VIBE	0.951 (0.837–0.986); $p < 0.001$	0.924 (0.747–0.979); $p < 0.001$	0.96 (0.867–0.989); $p < 0.001$	0.945 (0.817–0.985)
	UTE	0.808 (0.454–0.944); $p < 0.001$	0.783 (0.561–0.94); $p < 0.001$	0.828 (0.501–0.95); $p < 0.001$	0.806 (0.505–0.945)
Artifacts (ICC (95% CI); *p*–value)	DESS	0.911 (0.711–0.975); $p < 0.001$	0.942 (0.802–0.984); $p < 0.001$	0.905 (0.66–0.974); $p < 0.001$	0.919 (0.724–0.978)
	SPACE STIR	0.835 (0.699–0.937); $p < 0.001$	0.919 (0.732–0.977); $p < 0.001$	0.919 (0.732–0.977); $p < 0.001$	0.891 (0.721–0.964)
	SPACE SPAIR	0.96 (0.889–0.991); $p < 0.001$	0.931 (0.762–0.981); $p < 0.001$	0.965 (0.881–0.99); $p < 0.001$	0.952 (0.844–0.987)
	VIBE	0.939 (0.8–0.983); $p < 0.001$	0.939 (0.8–0.983); $p < 0.001$	0.939 (0.8–0.983); $p < 0.001$	0.939 (0.8–0.983)
	UTE	0.938 (0.796–0.983); $p < 0.001$	0.938 (0.796–0.983); $p < 0.001$	1	0.959 (0.796–0.983)
Root morphology (ICC (95% CI); *p*–value)	DESS	0.858 (0.716–0.932); $p < 0.001$	0.819 (0.62–0.913); $p < 0.001$	0.691 (0.433–0.844); $p < 0.001$	0.765 (0.59–0.896)
	SPACE STIR	0.782 (0.485–0.91); $p < 0.001$	0.783 (0.561–0.83); $p < 0.001$	0.763 (0.482–0.832); $p < 0.001$	0.776 (0.509–0.857)
	SPACE SPAIR	0.613 (0.387–0.796); $p < 0.001$	0.721 (0.423–0.89); $p < 0.001$	0.607 (0.381–0.765); $p < 0.001$	0.647 (0.397–0.817)
	VIBE	1	1	1	1
	UTE	1	1	1	1
Mandibular third molars evaluation					
Inferior alveolar nerve continuity score	DESS	1	1	1	1
	SPACE STIR	1	1	1	1
	SPACE SPAIR	1	1	1	1
	VIBE	0.948 (0.88–0.978); $p < 0.001$	1	1	0.983 (0.88–0.987)
	UTE	1	1	1	1
Nerve contact/non–contact	DESS	1	1	1	1
	SPACE STIR	1	1	1	1
	SPACE SPAIR	1	1	1	1
	VIBE	1	1	1	1
	UTE	1	1	1	1
Depth of impaction	DESS	0.867 (0.540–0.962); $p < 0.001$	0.766 (0.370–0.926); $p < 0.001$	0.867 (0.540–0.962); $p < 0.001$	0.833 (0.483–0.629)
	SPACE STIR	0.843 (0.480–0.94); $p < 0.001$	0.867 (0.540–0.962); $p < 0.001$	0.867 (0.540–0.962); $p < 0.001$	0.859 (0.52–0.955)
	SPACE SPAIR	0.867 (0.540–0.962); $p < 0.001$	0.766 (0.370–0.926); $p < 0.001$	0.766 (0.370–0.926); $p < 0.001$	0.8 (0.427–0.938)
	VIBE	0.766 (0.370–0.926); $p < 0.001$	1	0.766 (0.370–0.926); $p < 0.001$	0.844 (0.37–0.926)
	UTE	1	1	1	1
Ramus relationship	DESS	1	0.916 (0.708–0.976); $p < 0.001$	1	0.972 (0.708–0.976)
	SPACE STIR	1	1	1	1
	SPACE SPAIR	1	1	1	1
	VIBE	1	1	1	1
	UTE	1	0.945 (0.829–0.982); $p < 0.001$	1	0.982 (0.829–0.982)
Angulation of the third molar to the second molar	DESS	0.546 (−0.576–0.869); $p = 0.103$	0.605 (0.079–0.868); $p = 0.014$	0.747 (0.33–0.92); $p = 0.002$	0.633 (−0.056–0.886)
	SPACE STIR	0.656 (0.162–0.887); $p = 0.007$	0.319 (−1.367–0.804); $p = 0.268$	0.571 (−0.489–0.877); $p =$ 0–088	0.515 (1.694–0.856)
	SPACE SPAIR	0.766 (0.421–0.912); $p < 0.001$	0.656 (0.379–0.85); $p < 0.001$	0.683 (0.482–0.813); $p = 0.04$	0.702 (0.427–0.858)
	VIBE	1	1	1	1
	UTE	1	1	1	1
Maxillary third molars evaluation					
Positional relationship	DESS	0.933 (0.82–0.976); $p < 0.001$	1	0.933 (0.820–0.976); $p < 0.001$	0.955 (0.82–0.976)
	SPACE STIR	1	0.941 (0.846–0.978); $p < 0.001$	0.954 (0.873–0.984); $p < 0.001$	0.965 (0.86–0.981)

(*continued on next page*)

Table 3 (*continued*)

Agreement	MRI Sequence	Reader A and B	Reader B and C	Reader C and A	Average
	SPACE SPAIR	1	1	1	1
	VIBE	1	1	1	1
	UTE	1	1	1	1

nerve imaging prior to third molar surgery, because it provides high diagnostic confidence in identifying not only the inferior alveolar nerve but also the lingual nerve, and provides the performing surgeon with beneficial information that may allow for a more accurate, customized, and safer surgical approach (Al-Haj Husain et al., 2022c). The nerves appear as high-signal-intensity structures, reflecting the T2/T1 weighting of the PSIF echo signal, the increasing T2 specificity, and reduction signal decay due to dephasing, while at the same time the PSIF/echo contribution makes DESS MR-OPG susceptible to motion artifacts (Chavhan et al., 2008) (Fig. 1).

In this study setting, the use of mandibular coils achieved not only excellent high-contrast resolution images, but also minimized this type of artifact by providing comfortable fixation of the patient's head and jaw. However, DESS MR-OPG could enhance the detection of nerve fascicle disruptions, focal nerve size deviations, trace abnormalities, and the presence of other peripheral nerve-related disorders. The comparison of different fat suppression techniques (SPACE STIR and SPACE SPAIR) also confirmed good visualization of neural tissue in both sequences, with good diagnostic accuracy, but with lower image quality and higher artifact susceptibility compared with DESS (Figs. 2 and 3).

Data in the literature support these findings, and suggest that the overall SNR may be suboptimal in the third molar region, although a high contrast-to-noise ratio has been observed for space-occupying lesions in the region of interest (Burian et al., 2020a, 2020b). However, in the third molar region, SPACE-STIR protocols allow discrimination of the different components of the neurovascular bundle, because the blood vessels exhibit higher signal intensity than the neural tissue, potentially providing clinically useful preoperative data (Burian et al., 2020a).

In contrast to black bone MRI protocols, UTE and VIBE-Dixon provided the best image quality and low susceptibility to artifacts (Figs. 4 and 5). The UTE MR-OPGs provided superior diagnostic accuracy for anatomic visualization of hard tissues (cortical bone, tooth and root morphology, depth of impaction, ramus relationship, and angulation), while UTE and VIBE-Dixon MR-OPGs were less suitable for soft-tissue imaging. However, all these assessments were very robust and showed high reproducibility between the different readers. The combined use of high-field MRI and multichannel phased-array mandibular coils for UTE imaging with ultrashort hard-pulse excitation and three-dimensional center-put radial sampling provided appropriate image quality for visualization of the osseous structures and dental tissues, while reducing metal or field inhomogeneity artifacts (Du and Bydder, 2013; Manoliu et al., 2016). To the authors' best knowledge, there are only two pilot studies in the literature evaluating the use of MR-OPGs for visualization of the dento-maxillofacial complex (Assaf et al., 2014; Manoliu et al., 2016). Assaf et al. revealed the feasibility of creating panoramic reconstructions that can be used to visualize the pathoanatomy of various dental and osseous structures (Assaf et al., 2014). Manoliu et al.

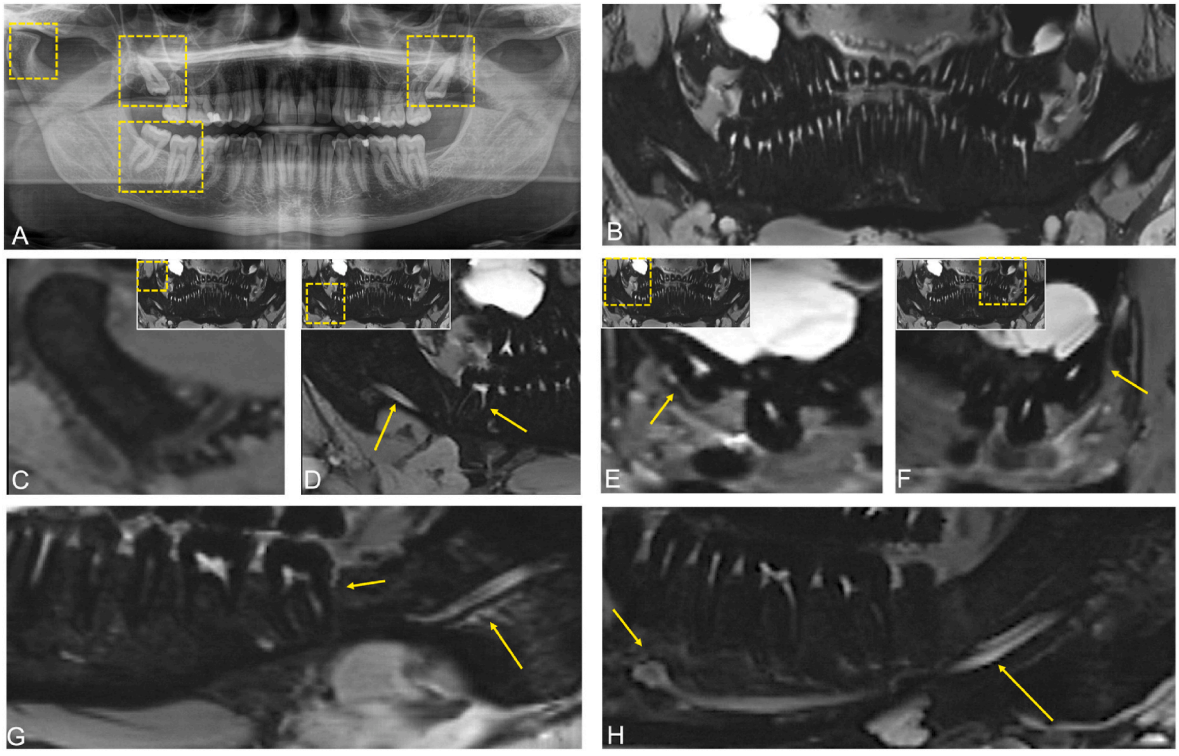

Fig. 1. A. X-ray-based OPG (orthopantomogram) and B. overview image of an OPG-like MRI reconstruction (MR-OPG) from a 3D double-echo steady-state dataset (DESS) dataset. C. Visualization of the temporomandibular joint, D. the course of the inferior alveolar nerve and partially impacted third molar (arrows pointing to it) in the E. first and F. second quadrant of a study participant's DESS MR-OPG. G. and H. Illustration of the intrabony course of the inferior alveolar nerve exhibiting T2-weighted hyperintense signals (long arrow), while the short arrow in G. marks the second molar in the third quadrant and in H. the emerging of the mental nerve from the mandible via the mental foramen.

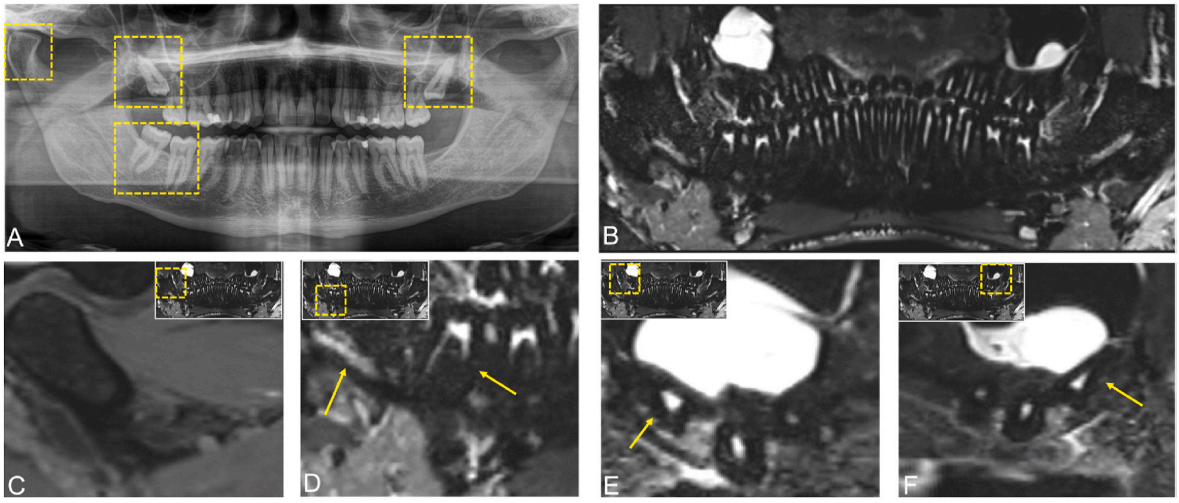

Fig. 2. A. X-ray-based OPG (orthopantomogram) and B. overview image of an OPG-like MRI reconstruction (MR-OPG) from a 3D fast spin echo short-tau inversion recovery (SPACE STIR) dataset. C. Visualization of the temporomandibular joint, D. the inferior alveolar nerve-third molar positional relationship, and partially impacted maxillary third molars (arrows pointing to it) in the E. first and F. second quadrant.

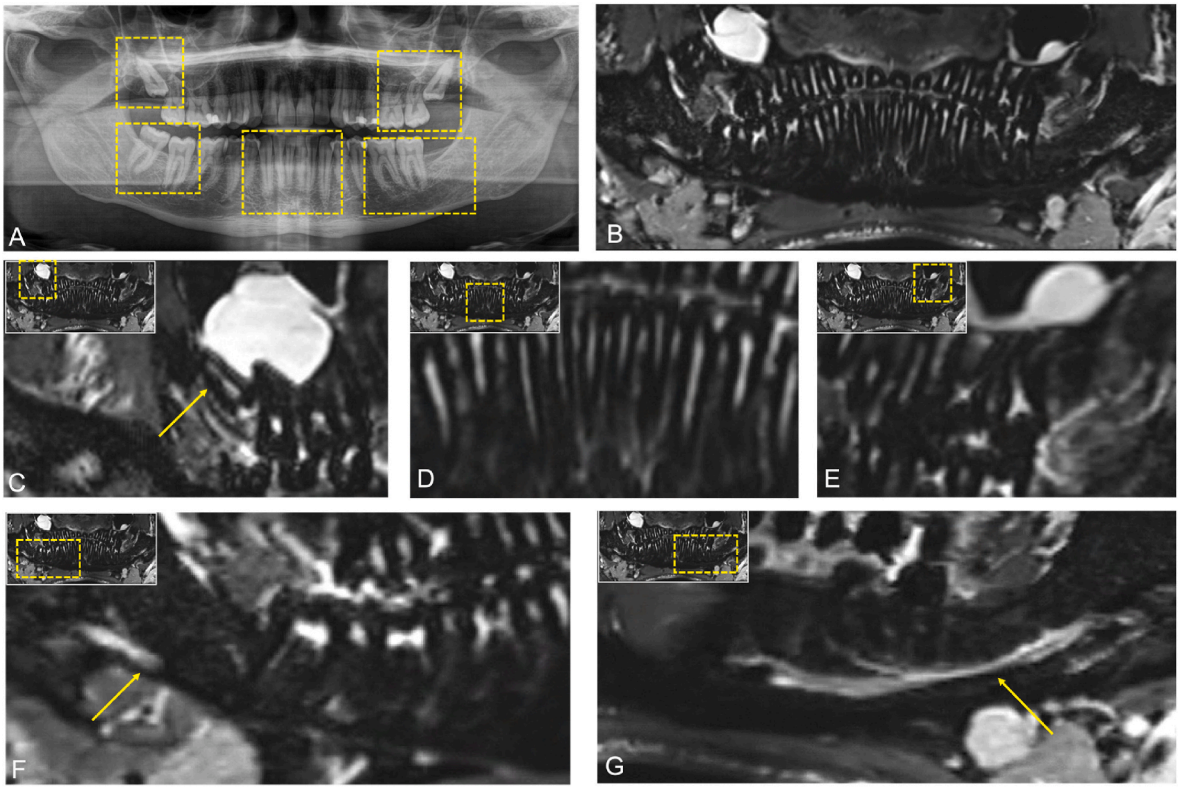

Fig. 3. A. X-ray-based OPG (orthopantomogram) and B. overview image of an OPG-like MRI reconstruction (MR-OPG) from a 3D fast spin echo spectral attenuated inversion recovery (SPACE-SPAIR) dataset. C. shows the positional relationship of the third molar in the first quadrant, while D. depicts the lower anterior teeth and E. the preoperative situation in the second quadrant. F. and G. show the neurovascular bundle and its course through the mandible in the region of interest.

described a novel MR neurography-OPG imaging technique in which UTE images of the dentomaxillofacial complex are overlaid with functional MR neurography using a 64-channel phased array coil, allowing assessment of the inferior alveolar nerves by fiber tractography, quantitative parameters, and diffusion properties (Manoliu et al., 2016). However, the main difficulties were inadequate segmental and continuous visualization of the thinnest peripheral nerves, long acquisition times, and susceptibility to artifacts. The use of mandibular coils and optimized MR protocols partially overcame these difficulties by allowing easier and faster data acquisition and MRI post processing with comparable or even better image quality.

Zero-echo time (ZTE) and UTE, which are capable of detecting signals from fast-decaying short-T2 components in tissue (Gatehouse and Bydder, 2003), have recently been increasingly used in the dental field, with promising results in segmentation and quantitative and qualitative assessment of cranial bones (Krämer et al., 2020), visualization of mineralized dental tissue (Stumpf et al., 2020), and in caries diagnosis, while there are still some limitations with dental fillings (Bracher et al.,

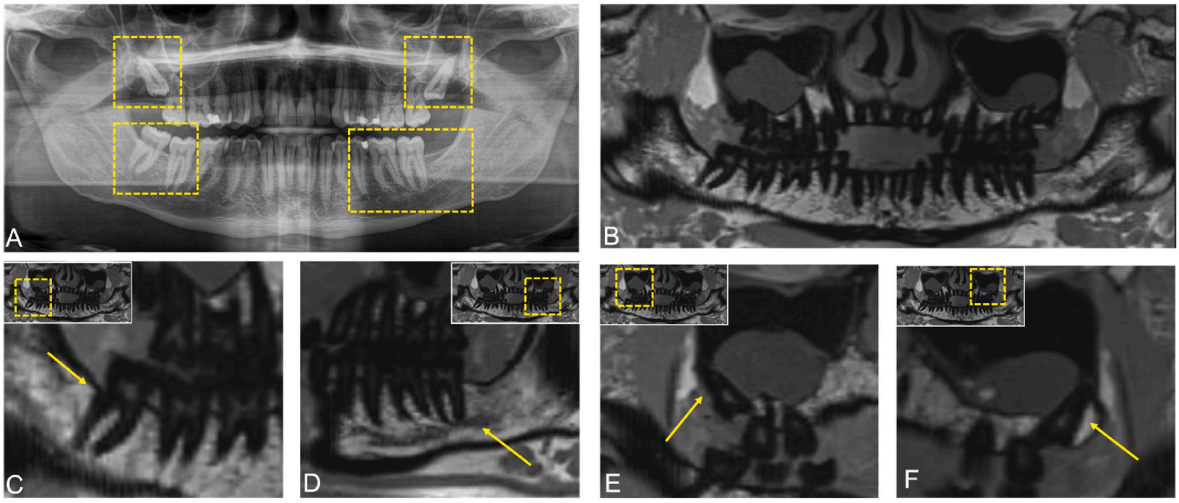

Fig. 4. A. X-ray-based OPG (orthopantomogram) and B. overview image of an OPG-like MRI reconstruction (MR-OPG) from a volumetric interpolated breath-hold examination (T1-VIBE-Dixon) dataset. C. shows the third molar positional relationship in the third quadrant, while D. displays the situation in the fourth quadrant. E. and F. show the preoperative positional relationship of teeth 18 and 28.

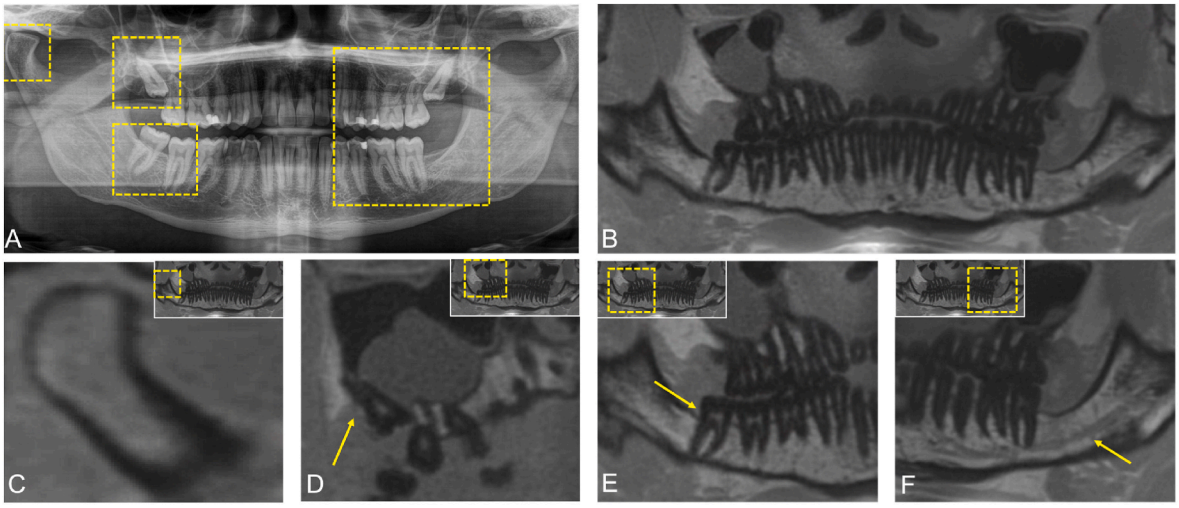

Fig. 5. A. X-ray-based OPG (orthopantomogram) and B. overview image of an OPG-like MRI reconstruction (MR-OPG) from an ultrashort-time-echo (UTE) dataset. C. Illustration of the temporomandibular joint, D. of the maxillary third molar in the first quadrant, and E. and F. highlighting the excellent visualization of the cortical and cancellous bone in the third molar region. The arrow in E. shows the inferior alveolar nerve-third molar relationship, while in F. it points to the intraosseous course of the inferior alveolar nerve.

2013). On the other hand, VIBE-Dixon MR-OPG can provide enhanced tissue characterization due to the acquired in-phase (water + fat) and out-of-phase (water − fat) images, and the generation of water-only (in-phase + counter-phase) and fat-only (in-phase − counter-phase) images (Suzuki et al., 2019). Therefore, not only can MRI be considered an ideal technique for depicting inflammatory soft-tissue disorders due its increased water content (Schara et al., 2009), but it is also suitable for imaging bony lesions and tumor progression originating from the mandible or maxilla (Eley et al., 2014).

Regarding quantitative parameters relevant to third molar surgery, MR OPGs revealed no significant differences compared with radiographic OPGs, confirming previously published data according to which MRI is useful for visualizing various anatomical structures in the head and neck region, as well as pathologies, and can be even considered a reliable predictor of neoplasm outcome (Boland et al., 2010; Eley et al., 2013, 2014). In terms of qualitative parameters, it can be concluded that black bone MR-OPGs are excellent for obtaining optimal soft tissue/-bone contrast, but that in regions where craniofacial bone structures are adjacent to air, discrimination can be difficult (Eley et al., 2012). UTE and VIBE-Dixon are superior in assessing positional relationships and root morphology, and offer excellent overall image quality, lower artifact susceptibility in the oral cavity, and shorter acquisition times. In contrast, no significant difference was found between the performance of black bone MRI and UTE and VIBE-Dixon in assessing the nerve contact/non-contact relationship. Therefore, MR-OPG represents a valuable radiation-free imaging modality that has the potential to eliminate exposure to X-rays in oral and maxillofacial imaging in specific indications, thereby reducing the incidence of radiation-induced cancer from the use of CBCTs in dentistry (Petersen et al., 2015).

Several limitations should be mentioned with regard to the methodology of this pilot study. First, the sample size of 11 patients (representing 31 third molars) did not allow the drawing of general conclusions, since selection bias cannot be ruled out. Therefore, more significant cohorts and additional studies are necessary to generate further evidence on MR-OPG. Second, data acquisition remained challenged by the occurrence of artifacts caused by dental restorations or

orthodontic applications. In this study, the sources of artifacts were not evaluated, but the occurrence of different types of artifact in general was classified. This aspect should be investigated in more detail in further studies. The somewhat longer scan times — up to 12 min for specific sequences — and the limited availability of MRI scanners remain barriers that need to be addressed, and will require further improvement for use in clinical practice.

5. Conclusion

High-field MR scanners, dedicated MR sequences, and the use of a 15-channel mandibular coil allow the acquisition of radiation-free MR-OPGs for preoperative diagnosis in third molar surgery within clinically tolerable acquisition times. Surgical procedures on third molars could be planned in indicated cases with MR-OPG, which exhibited high image quality and low susceptibility to artifacts. No significant difference was observed between MR-OPG and X-ray-based OPG with regard to the assessment of quantitative parameters. UTE MR-OPG (acquisition time 3 min) provided radiographic-like images and was best suited for assessing preoperative data relevant to third molar surgery, such as positional relationship, contact/non-contact of the inferior alveolar nerve, and dental root morphology. For continuous and focal imaging of the inferior alveolar nerve and lingual nerve, DESS MR-OPG was most suited. Therefore, not every MR-OPG protocol could be appropriate for every clinical case, suggesting a shift towards indication-specific and modality-oriented perioperative imaging, leading to potentially improved perioperative case management, especially in high-risk surgeries.

Author contributions

Conceptualization and design — AAH, DAO, BS, SW, MÖ, DS, NAH, SS, MP, SV; acquisition of data, or analysis and interpretation of data — AAH, DAO, BS, SW, MP, SS, SV; statistics — AAH, MÖ;, NAH; drafting of manuscript — AAH and DAO; writing, reviewing, and editing —; BS, SW, MÖ;, DS, NAH, SS, MP, SV. All authors read and agreed to the published version of the manuscript. All authors agreed to be accountable for all aspects of the work.

Data availability statement

The datasets used during and/or analyzed during the current study are available from the corresponding author on request.

Financial disclosure

None.

Funding

None.

Declaration of competing interest

The authors declare no competing interests.

References

Al-Haj Husain, A., Sekerci, E., Schönegg, D., Bosshard, F.A., Stadlinger, B., Winklhofer, S., Piccirelli, M., Valdec, S., 2022a. Dental MRI of oral soft-tissue tumors — optimized use of black bone MRI sequences and a 15-channel mandibular coil. J. Imag. 8.

Al-Haj Husain, A., Solomons, M., Stadlinger, B., Pejicic, R., Winklhofer, S., Piccirelli, M., Valdec, S., 2021b. Visualization of the inferior alveolar nerve and lingual nerve using MRI in oral and maxillofacial surgery: a systematic review. Diagnostics 11.

Al-Haj Husain, A., Stadlinger, B., Winklhofer, S., Piccirelli, M., Valdec, S., 2022b. Magnetic resonance imaging for preoperative diagnosis in third molar surgery: a systematic review. Oral Radiol. https://pubmed.ncbi.nlm.nih.gov/35397042/.

Al-Haj Husain, A., Valdec, S., Stadlinger, B., Rucker, M., Piccirelli, M., Winklhofer, S., 2022c. Preoperative visualization of the lingual nerve by 3D double-echo steady-state MRI in surgical third molar extraction treatment. Clin. Oral Invest. 26, 2043–2053.

Andreisek, G., Chhabra, A., 2015. MR neurography: pitfalls in imaging and interpretation. Semin. Muscoskel. Radiol. 19, 94–102.

Assaf, A.T., Zrnc, T.A., Remus, C.C., Schönfeld, M., Habermann, C.R., Riecke, B., Friedrich, R.E., Fiehler, J., Heiland, M., Sedlacik, J., 2014. Evaluation of four different optimized magnetic-resonance-imaging sequences for visualization of dental and maxillo-mandibular structures at 3 T. J. Cranio-Maxillo-Fac. Surg. 42, 1356–1363.

Boland, P.W., Watt-Smith, S.R., Pataridis, K., Alvey, C., Golding, S.J., 2010. Evaluating lingual carcinoma for surgical management: what does volumetric measurement with MRI offer? Br. J. Radiol. 83, 927–933.

Bracher, A.K., Hofmann, C., Bornstedt, A., Hell, E., Janke, F., Ulrici, J., Haller, B., Geibel, M.A., Rasche, V., 2013. Ultrashort echo time (UTE) MRI for the assessment of caries lesions. Dentomaxillofacial Radiol. 42, 20120321.

Burian, E., Probst, F.A., Weidlich, D., Cornelius, C.P., Maier, L., Robl, T., Zimmer, C., Karampinos, D.C., Ritschl, L.M., Probst, M., 2019. MRI of the inferior alveolar nerve and lingual nerve — anatomical variation and morphometric benchmark values of nerve diameters in healthy subjects. Clin. Oral Invest.

Burian, E., Probst, F.A., Weidlich, D., Cornelius, C.P., Maier, L., Robl, T., Zimmer, C., Karampinos, D.C., Ritschl, L.M., Probst, M., 2020a. MRI of the inferior alveolar nerve and lingual nerve — anatomical variation and morphometric benchmark values of nerve diameters in healthy subjects. Clin. Oral Invest. 24, 2625–2634. https://pubmed.ncbi.nlm.nih.gov/31705309/.

Burian, E., Sollmann, N., Ritschl, L.M., Palla, B., Maier, L., Zimmer, C., Probst, F., Fichter, A., Miloro, M., Probst, M., 2020b. High resolution MRI for quantitative assessment of inferior alveolar nerve impairment in course of mandible fractures: an imaging feasibility study. Sci. Rep. 10, 11566.

Chang, E.Y., Du, J., Chung, C.B., 2015. UTE imaging in the musculoskeletal system. J. Magn. Reson. Imag. 41, 870–883.

Chavhan, G.B., Babyn, P.S., Jankharia, B.G., Cheng, H.L., Shroff, M.M., 2008. Steady-state MR imaging sequences: physics, classification, and clinical applications. Radiographics 28, 1147–1160.

Du, J., Bydder, G.M., 2013. Qualitative and quantitative ultrashort-TE MRI of cortical bone. NMR Biomed. 26, 489–506.

Dula, K., Bornstein, M.M., Buser, D., Dagassan-Berndt, D., Ettlin, D.A., Filippi, A., Gabioud, F., Katsaros, C., Krastl, G., Lambrecht, J.T., Lauber, R., Luebbers, H.T., Pazera, P., Türp, J.C., SADMFR, 2014. SADMFR guidelines for the use of cone-beam computed tomography/digital volume tomography. Swiss Dent. J 124, 1169–1183.

Eley, K.A., McIntyre, A.G., Watt-Smith, S.R., Golding, S.J., 2012. 'Black bone' MRI: a partial flip angle technique for radiation reduction in craniofacial imaging. Br. J. Radiol. 85, 272–278.

Eley, K.A., Watt-Smith, S.R., Boland, P., Potter, M., Golding, S.J., 2014. MRI pre-treatment tumour volume in maxillary complex squamous cell carcinoma treated with surgical resection. J. Cranio-Maxillo-Fac. Surg. 42, 119–124.

Eley, K.A., Watt-Smith, S.R., Golding, S.J., 2013. Magnetic resonance imaging-based tumor volume measurements predict outcome in patients with squamous cell carcinoma of the mandible. Oral Surg. Oral Med. Oral Pathol. Oral Radiol. 115, 255–262.

Fujii, H., Fujita, A., Yang, A., Kanazawa, H., Buch, K., Sakai, O., Sugimoto, H., 2015. Visualization of the peripheral branches of the mandibular division of the trigeminal nerve on 3D double-echo steady-state with water excitation sequence. AJNR Am. J. Neuroradiol. 36, 1333–1337.

Gatehouse, P.D., Bydder, G.M., 2003. Magnetic resonance imaging of short T2 components in tissue. Clin. Radiol. 58, 1–19.

Guggenberger, R., Winklhofer, S., Osterhoff, G., Wanner, G.A., Fortunati, M., Andreisek, G., Alkadhi, H., Stolzmann, P., 2012. Metallic artefact reduction with monoenergetic dual-energy CT: systematic ex vivo evaluation of posterior spinal fusion implants from various vendors and different spine levels. Eur. Radiol. 22, 2357–2364.

Hwang, S.Y., Choi, E.S., Kim, Y.S., Gim, B.E., Ha, M., Kim, H.Y., 2018. Health effects from exposure to dental diagnostic X-ray. Environ/ Health Toxicol/ 33, e2018017.

Idiyatullin, D., Corum, C., Moeller, S., Prasad, H.S., Garwood, M., Nixdorf, D.R., 2011. Dental magnetic resonance imaging: making the invisible visible. J. Endod. 37, 745–752.

Jerjes, W., Swinson, B., Moles, D.R., El-Maaytah, M., Banu, B., Upile, T., Kumar, M., Al Khawalde, M., Vourvachis, M., Hadi, H., Kumar, S., Hopper, C., 2006. Permanent sensory nerve impairment following third molar surgery: a prospective study. Oral Surg. Oral Med. Oral Pathol. Oral Radiol. Endod. 102, e1–e7.

Jung, Y.H., Cho, B.H., 2015. Assessment of maxillary third molars with panoramic radiography and cone-beam computed tomography. Imag. Sci. Dent. 45, 233–240.

Koo, T.K., Li, M.Y., 2016. A guideline of selecting and reporting intraclass correlation coefficients for reliability research. J. Chiropr. Med. 15, 155–163.

Krämer, M., Herzau, B., Reichenbach, J.R., 2020. Segmentation and visualization of the human cranial bone by T2* approximation using ultra-short echo time (UTE) magnetic resonance imaging. Z. Med. Phys. 30, 51–59.

Ludwig, U., Eisenbeiss, A.K., Scheifele, C., Nelson, K., Bock, M., Hennig, J., von Elverfeldt, D., Herdt, O., Flügge, T., Hövener, J.B., 2016. Dental MRI using wireless intraoral coils. Sci. Rep. 6, 23301.

Manoliu, A., Ho, M., Nanz, D., Dappa, E., Boss, A., Grodzki, D.M., Liu, W., Chhabra, A., Andreisek, G., Kuhn, F.P., 2016. MR neurographic orthopantomogram: ultrashort echo-time imaging of mandibular bone and teeth complemented with high-resolution morphological and functional MR neurography. J. Magn. Reson. Imag. 44, 393–400.

Pell, G., Gregory, G.J., 1933. Impacted third molars: classification and modified technique for removal. Dent. Digest 39, 330–338.

Petersen, L.B., Olsen, K.R., Matzen, L.H., Vaeth, M., Wenzel, A., 2015. Economic and health implications of routine CBCT examination before surgical removal of the mandibular third molar in the Danish population. Dentomaxillofacial Radiol. 44, 20140406.

Prager, M., Heiland, S., Gareis, D., Hilgenfeld, T., Bendszus, M., Gaudino, C., 2015. Dental MRI using a dedicated RF-coil at 3 tesla. J. Cranio-Maxillo-Fac. Surg. 43, 2175–2182.

Qi, W., Lei, J., Liu, Y.N., Li, J.N., Pan, J., Yu, G.Y., 2019. Evaluating the risk of post-extraction inferior alveolar nerve injury through the relative position of the lower third molar root and inferior alveolar canal. Int. J. Oral Maxillofac. Surg. 48, 1577–1583.

Schara, R., Sersa, I., Skaleric, U., 2009. T1 relaxation time and magnetic resonance imaging of inflamed gingival tissue. Dentomaxillofacial Radiol. 38, 216–223.

Stumpf, K., Kaye, E., Paul, J., Wundrak, S., Pauly, J.M., Rasche, V., 2020. Two-dimensional UTE overview imaging for dental application. Magn. Reson. Med. 84, 2616–2624.

Suzuki, N., Kuribayashi, A., Sakamoto, K., Sakamoto, J., Nakamura, S., Watanabe, H., Harada, H., Kurabayashi, T., 2019. Diagnostic abilities of 3T MRI for assessing mandibular invasion of squamous cell carcinoma in the oral cavity: comparison with 64-row multidetector CT. Dentomaxillofacial Radiol. 48, 20180311.

Tsapaki, V., 2017. Radiation protection in dental radiology — recent advances and future directions. Phys. Med. 44, 222–226.

Valdec, S., Al-Haj Husain, A., Winklhofer, S., Müller, M., Piccirelli, M., Stadlinger, B., 2021. Comparison of preoperative cone-beam computed tomography and 3D-double echo steady-state MRI in third molar surgery. J. Clin. Med. 10.

Winter, G., 1926. Principles of Exodontia as Applied to the Impacted Third Molars. American Medical Book Company, St. Louis.

Yilmaz, S., Adisen, M.Z., Misirlioglu, M., Yorubulut, S., 2016. Assessment of third molar impaction pattern and associated clinical symptoms in a central Anatolian Turkish population. Med. Princ. Pract. 25, 169–175.